THE ASTROPHYSICAL JOURNAL, 518:1002–1009, 1999 June 20

LABORATORY MEASUREMENTS OF Fe XXIV LINE EMISSION: $3 \rightarrow 2$ TRANSITIONS NEAR EXCITATION THRESHOLD

M. F. GU, S. M. KAHN, AND D. W. SAVIN
Department of Physics and Columbia Astrophysics Laboratory, Columbia University, New York, NY 10027
P. BEIERSDORFER, G. V BROWN, D. A. LIEDAHL, AND K. J. REED
Department of Physics and Space Technology, Lawrence Livermore National Laboratory, Livermore CA 94550
AND
C. P. BHALLA AND S. R. GRABBE
Department of Physics, Kansas State University, Manhattan, KS 66506
Received 1998 November 20; accepted 1999 January 25

ABSTRACT

Using the Electron Beam Ion Trap facility at Lawrence Livermore National Laboratory, we have measured relative cross sections for Fe XXIV line emission at electron energies between 0.7 and 3.0 keV. The measurements include line formation by direct electron impact excitation (DE), radiative cascades, resonant excitation (RE), and dielectronic recombination (DR) satellites with captured electrons in $n \geq 5$ levels. Good agreement with *R*-matrix and distorted wave calculations is found. In collisionally ionized plasmas, at temperatures near where the ion abundance peaks ($kT_e \sim 1.7$ keV), the RE contributions are found to be $\lesssim 5\%$ of the line emission, while the DR satellites contribute $\lesssim 10\%$. While good agreement with state-of-the-art atomic physics calculations is found, there is less good agreement with existing spectral synthesis codes in common astrophysical use. For the Fe XXIV $3p_{3/2} \rightarrow 2s_{1/2}$, $3p_{1/2} \rightarrow 2s_{1/2}$, and $3d_{5/2} \rightarrow 2p_{3/2}$ transitions, the synthesis code MEKAL underestimates the emissivity in coronal equilibrium by $\sim 20\%$ at temperatures near where the ion abundance peaks. In situations where the ionization balance is not solely determined by the electron temperature, RE and DR satellites may contribute a considerable fraction of the line emission.

Subject headings: atomic data — atomic processes — line: formation — methods: laboratory — X-rays: general

1. INTRODUCTION

Spectroscopy is the primary tool for probing the physical conditions in astronomical X-ray sources. Among all the atomic species contributing discrete spectroscopic features at X-ray energies (0.1–10 keV), iron ions have drawn the most attention because iron has the highest cosmic abundance for a high-*Z* element and iron ions emit prominently over a wide temperature range. The iron K-shell transitions have been observed from many astrophysical environments with *ASCA* (Makino & Mitsuda 1997) and have provided a wealth of information about the physical processes occurring there. However, there are many important situations where iron L-shell ions dominate the X-ray emission, such as in collisional plasmas with temperatures <2 keV. Because these ions are multielectron systems, the L-shell spectra are generally richer than K-shell spectra from the H-like and He-like ions that coexist with iron L-shell ions and provide more diagnostic information about the emitting sources (Kahn & Liedahl 1990).

Resolving the complicated structure of iron L-shell spectra ($\sim$6–18 Å) demands high spectral resolution. This will be achieved in the next few years when the *Advanced X-ray Astrophysics Facility* (*AXAF*), the *X-Ray Multimirror Mission* (*XMM*), and *Astro-E* are launched. These satellites will carry spectrometers with resolving powers in the iron L region over an order of magnitude greater than those of the spectrometers aboard *ASCA*. However, reliable interpretation of the collected spectra will also require accurate atomic physics data for the various observed transitions. For the strongest observed lines in the spectral region of interest (typically allowed transitions) and with not too high density (coronal approximation is valid), the upper level radiatively decays (with a typical rate of $\gtrsim 10^9$ s^{-1}) before it is collisionally deexcited. Hence, radiative transition probabilities are not as important as collisional excitation rates. Calculations of relevant collision rates have been produced nearly continuously over the last few decades. Although reasonable accuracy has been achieved for simple K-shell ions, considerable uncertainties still exist for the more complex L-shell ions. Even with the moderate spectral resolution of *ASCA*, several observations have shown discrepancies between observed cosmic spectra and available spectral models. For example, Arimoto et al. (1997) found that the iron abundances of the interstellar medium (ISM) in elliptical galaxies derived from the iron L spectra vary significantly when different spectral codes are used. In addition, Fabian et al. (1994) showed that the $4 \rightarrow 2$ line emission of Fe XXIII and Fe XXIV relative to the $3 \rightarrow 2$ line emission are overpredicted by all standard plasma emission codes when compared to the observed *ASCA* spectrum of the Centaurus cluster of galaxies.

The results of Fabian et al. led to new calculations of Fe XXIII and Fe XXIV electron impact excitation (EIE) rate coefficients (Liedahl, Osterheld, & Goldstein 1995) using the distorted wave (DW) Hebrew University Lawrence Livermore Atomic Code (HULLAC). These calculations alleviate the poor fit of the *ASCA* data. Using the Lawrence Livermore Electron Beam Ion Trap (EBIT), our group (Savin et al. 1996) previously measured the relative line emission of several Fe XXIV $3 \rightarrow 2$ and $4 \rightarrow 2$ lines and found good agree-

ment with both the HULLAC calculations and fully relativistic DW calculations using the code of Zhang, Sampson, & Clark (1990a). These measurements, however, were done at electron energies significantly above the excitation threshold energies of the lines observed and away from any resonances that could produce $3 \rightarrow 2$ or $4 \rightarrow 2$ line emission. In that range, the DW approximation is justified. At energies near threshold, on the other hand, DW is expected to break down and one expects to find rich resonance structure, as illustrated by recent *R*-matrix calculations of Fe XXIV (Berrington & Tully 1997). To provide a benchmark for these various calculations and to study the effects of resonances, we have extended our measurements of Fe XXIV $3 \rightarrow 2$ line emission with EBIT to the near threshold regime, $\sim$0.7–3.0 keV. In this paper, we present the relative cross sections for producing the strongest lines in the L-shell spectrum of Fe XXIV. In particular, we measured the $3d_{5/2} \rightarrow 2p_{3/2}$ line at $\lambda = 11.18$ Å, the $3p_{3/2} \rightarrow 2s_{1/2}$ line at $\lambda = 10.62$ Å, the $3p_{1/2} \rightarrow 2s_{1/2}$ line at $\lambda = 10.66$ Å, and the associated Fe XXIII satellite lines produced by dielectronic recombination (DR) that blend with these features.

Various processes contribute to the line emission observed from a collisional plasma. Direct excitation (DE) dominates at energies above the EIE threshold. Resonant excitation (RE) can populate the same levels as DE via dielectronic capture followed by autoionization to the level of interest. Below the EIE threshold, DR onto Fe XXIV produces high n satellites that cannot be resolved from the main lines. In this work, we have observed the following processes:

$$\text{DE: } Fe^{23+}(2s) + e^- \rightarrow Fe^{23+}(3l) + e^- \rightarrow Fe^{23+}(2s) + h\nu_1 + e^-,$$

$$\text{RE: } Fe^{23+}(2s) + e^- \rightarrow Fe^{22+}(4l'nl'') \rightarrow Fe^{23+}(3l) + e^- \rightarrow Fe^{23+}(2s) + h\nu_1 + e^-, \quad \text{and}$$

$$\text{DR: } Fe^{23+}(2s) + e^- \rightarrow Fe^{22+}(3lnl') \rightarrow Fe^{22+}(2snl') + h\nu_2,$$

with $l = p$ and d. Quantum mechanically, there is no way to distinguish between DE and RE, and we measure the coherent sum of the two processes. DR satellites involving capture into levels with $n \geq 5$ are not resolved spectroscopically from the corresponding Fe XXIV lines in our measurements. However, their contributions occur at electron energies below the EIE thresholds and are thus easily distinguishable from DE and RE.

This paper is organized as follows. Our experimental and data analysis techniques are presented in § 2 and § 3, respectively. In § 4, we present our results, and in § 5, we discuss the significance and implications of the measurements. A summary and conclusions are given in § 6.

2. EXPERIMENTAL TECHNIQUE

EBIT (Levine et al. 1988) uses a magnetically confined electron beam to produce a potential well that traps the ions in the radial direction. In the axial direction, ions are trapped electrostatically by a positive bias applied to the top and bottom drift tubes. The electron beam is also used to ionize and excite the trapped ions. This device is unique in its ability to measure line formation processes of highly charged ions, including indirect processes such as radiative cascades and resonant excitation (Beiersdorfer et al. 1990), because spectral radiation produced under well-controlled conditions can be directly observed with high-resolution spectrometers. In the present measurements, the resulting X-ray emission is observed by two flat crystal spectrometers (FCS) (Beiersdorfer & Warglin 1994; Beiersdorfer et al. 1997; Brown, Beiersdorfer, & Widmann 1998) through X-ray ports. Thallium acid phthalate crystals [TAP(001)] are used in both spectrometers. The spectrometers are set to observe the same spectral region in order to increase the statistics. The dispersion planes of the spectrometers are perpendicular to the electron beam. Between EBIT and each FCS is a thin window (0.5 μm Mylar window in one spectrometer and a 0.5 μm Lexan window in the other). X-rays are detected by position-sensitive proportional counters with 4 μm polypropylene windows.

Low-charge states of iron are formed using a metal vapor vacuum arc source (Brown et al. 1986) and injected into EBIT. After injection, the beam energy is held at 3 keV for $\sim$350 ms and is then varied according to the timing pattern shown in Figure 1. We collect data as the beam energy is linearly swept between $\sim$0.7 and 3.0 keV. By time-tagging the detected X-ray signal, we can then associate each emitted photon with a particular electron energy. The intensity of a given line observed by the crystal spectrometer at beam energy E is proportional to the quantity

$$G(E)\sigma(E)v(E)TD\int n_e(\boldsymbol{r})n_q(\boldsymbol{r})d^3\boldsymbol{r}\,, \tag{1}$$

where the integration is over the trap volume, $n_e(\boldsymbol{r})$ is the electron density, $n_q(\boldsymbol{r})$ is the ion density of charge state q, σ is the cross section for producing the observed line emission, v is the electron velocity, T is the transmittance of the windows, D is the detector efficiency, and $G(E)$ is a correction factor accounting for the polarization and anisotropy of the radiation. For electric dipole transitions such as those measured here,

$$G(E) = [(1 + P) + (1 - P)f]\,\frac{3}{3 - P}\,, \tag{2}$$

where $f = R_\pi/R_\sigma$. R_π and R_σ are the integrated reflectivities of the crystal for radiation polarized, respectively, along the dispersion plane and perpendicular to the dispersion plane

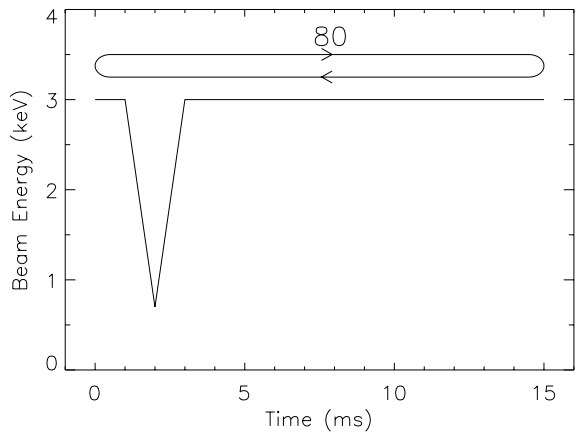

FIG. 1.—Timing pattern used in the present measurements. After the ion injection, the beam energy is kept at 3.0 keV for 350 ms. It is then varied according to the pattern shown in the figure. The entire cycle of 15 ms is repeated 80 times before dumping the trapped ions.

(Beiersdorfer et al. 1992), and P is the polarization parameter, which is defined as

$$P = \frac{I_\sigma - I_\pi}{I_\sigma + I_\pi}, \quad (3)$$

where I_π and I_σ are, respectively, the intensities of emitted radiation polarized along the dispersion plane and perpendicular to the dispersion plane (Percival & Seaton 1958).

During the sweeping of the beam energy, the charge balance changes insignificantly because the ionization and recombination timescales at these energies are much longer than the time spent to sweep the beam energy. In order to maintain a constant electron density, we vary the beam current synchronously with the beam energy. The integral involving the electron density and the ion density therefore stays constant as the beam energy changes. We have no tight constraint on the explicit value of this integral, so we are unable to make absolute measurements of the individual line cross sections. However, we can normalize our results to the theoretical cross sections of a particular line in an energy range where the calculations are believed to be least uncertain.

3. DATA ANALYSIS

The data have been collected using an event-mode data acquisition scheme (Knapp et al. 1993) in which the photon energy, the electron beam energy, and the time of each event are recorded. Figure 2 shows a representative scatter plot of the beam energy versus the photon wavelength, and a summed spectrum of the data. The beam energy spread is 35 ± 5 eV (see § 4). The spectrometer resolving power $E/\Delta E$ is ~ 250. X-ray emission lines appear as vertical lines in this plot, and the bright spots on the lines are due to resonances. Spectra collected without iron in the trap show no background lines that might blend with the Fe XXIV lines of interest. Spectra taken at different beam energies are analyzed separately to get the line intensities versus beam energy. A number of corrections are then applied in calculating the cross sections.

First, some background emission is observed at beam energies below the EIE thresholds and away from DR resonances. The background is mostly due to radiative recombination (RR) and charge transfer (CT) of Fe^{24+}, which populate excited levels of Fe^{23+}. The ionization balance determined from various observed and theoretical line ratios of different iron charge states shows that CT is the dominant recombination mechanism in our energy region. A uniform background is subtracted from the observed intensities, since CT is beam energy independent and the time spent at each energy was the same.

The polarizations of $3d_{5/2} \rightarrow 2p_{3/2}$ and $3p_{3/2} \rightarrow 2s_{1/2}$ are beam-energy dependent. Using the code of Zhang et al. (1990a), the magnetic level specific cross sections are calculated to obtain the polarization factors at electron energies above 1.5 keV. At energies between EIE thresholds and 1.5 keV, we have carried out extensive R-matrix calculations to take into account the effects of RE. The results above EIE thresholds, excluding RE effects, are then extrapolated below the relevant thresholds to obtain the polarization factors of the DR satellites since they are expected to match the polarizations of DE at threshold (Inal & Dubau 1989). In calculating the correction factor $G(E)$, f is taken to be the average of the predicted value for ideally perfect crystals

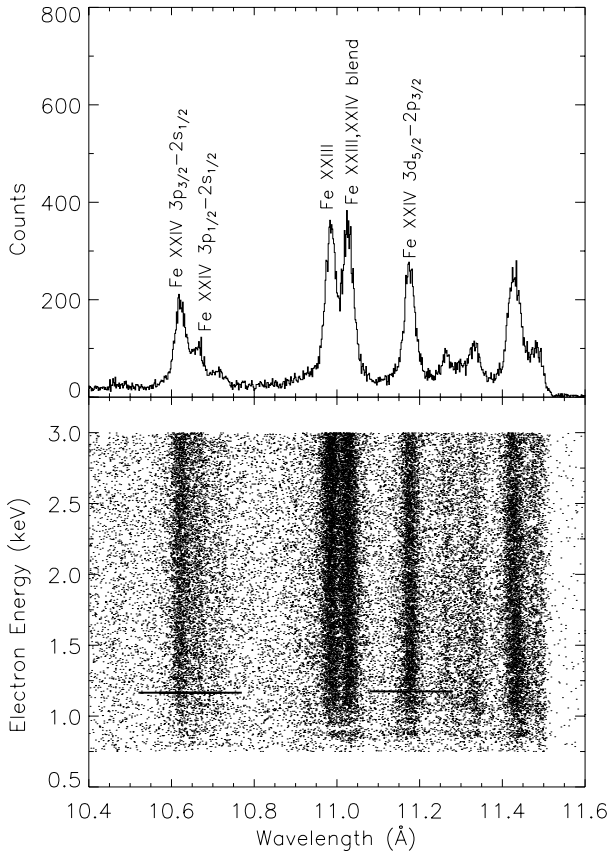

FIG. 2.—Lower panel shows a representative scatter plot in which each point represents a photon. The x-axis is its wavelength and the y-axis is the energy of the electron that produces the photon. The horizontal lines indicate the EIE thresholds for producing the three Fe XXIV transitions of interest here. At electron energies below the thresholds, the line emission is due to DR satellites. The upper panel shows the collapsed spectrum corresponding to the scatter plot in the lower panel. The transitions of interest here are labeled. Unlabeled lines are due to various Fe lines and background lines

with absorption (Henke, Gullikson, & Davis 1993) and for ideally mosaic crystals ($f = \cos^2 2\theta_B$, where θ_B is the Bragg angle). For a realistic crystal, f lies between these two extremes, which here differ by $\lesssim 6\%$ in the wavelength band concerned. We therefore infer that the uncertainty in f should be $\lesssim 6\%$. An additional complication in calculating these polarization corrections is that the electrons in EBIT have a nonnegligible transverse energy $E_\perp \sim 200$ eV (Beiersdorfer et al. 1992). The polarization is related to that due to a nonspiraling beam by

$$P = P_0 \frac{1 - 3E_\perp/2E}{1 - P_0 E_\perp/2E}, \quad (4)$$

where P_0 is the polarization for a nonspiraling beam (Gu, Savin, & Beiersdorfer 1998). This effect may decrease the polarization by as much as 30% at energies below 1 keV. However, we note that $G(E)$ is not strongly sensitive to P and f. For the case of $3d_{5/2} \rightarrow 2p_{3/2}$ and $3p_{3/2} \rightarrow 2s_{1/2}$ transitions at energies ~ 1 keV, for example, 30% errors in P and 6% errors in f result in $\sim 8\%$ and $\sim 1\%$ errors in $G(E)$, respectively. The $3p_{1/2} \rightarrow 2s_{1/2}$ transition is unpolarized, and hence the correction factor does not depend on energy. A 6% error in f introduces only a $\lesssim 2\%$ error in the normalization level for this transition.

TABLE 1

UNCERTAINTIES FOR MEASURED CROSS SECTIONS

	$3p_{3/2} - 2s_{1/2}$ (%)[b]				$3p_{1/2} \rightarrow 2s_{1/2}$ (%)[b]				$3d_{5/2} \rightarrow 2p_{3/2}$ (%)[b]			
Source[a]	<1.0 (keV)	1.0–1.5 (keV)	1.5–3.0 (keV)	Norm.	<1.0 (keV)	1.0–1.5 (keV)	1.5–3.0 (keV)	Norm.	<1.0 (keV)	1.0–1.5 (keV)	1.5–3.0 (keV)	Norm.
Statistics	17	16	6	5	30	30	10	8	10	10	4	0
Polarization	8	2	2	2	0	0	0	2	8	2	2	0
Overlap	10	6	6	6	10	6	6	6	10	6	6	0
Line Blend	0	0	0	2	0	0	0	2	2	2	2	0
Transmittance.....	0	0	0	4	0	0	0	4	0	0	0	0
Quad. Sum	21	17	12	9	32	30	12	11	20	11	8	0

[a] The meaning of various source terms is as following: the values in the first row are statistical uncertainties which include those introduced by the background subtraction; the values in the second row are due to the polarization correction factor; the values in the third row are due to the beam-ion overlap integral; the values in the fourth row are due to line bends; the values in the fifth row are due to the window transmittances; and the values in the last row are the quadrature sum. All uncertainties are quoted at the 1 σ level.

[b] For each transition, the typical uncertainties at beam energies below 1.0 keV are in the first column, those from 1.0 to 1.5 keV are in the second column, and those from 1.5 to 3.0 keV are in the third column. In the fourth column are the uncertainties in the normalization level that shift the entire data set without changing its shape. Since the $3d_{5/2} \rightarrow 2p_{3/2}$ transition is chosen as normalization, its normalization error is 0.

We have checked how well we can maintain a constant overlap integral $\int n_e(r)n_q(r)d^3r$ versus beam energy by measuring the RR signals onto the K-shell of Ar^{17+} and Ar^{18+} while linearly sweeping the beam energy. The RR cross sections have been calculated using a Hartree-Slater model (Scofield 1989, 1991) that is in good agreement with photoionization experiments (Saloman, Hubbel, & Scofield 1988). Hence the change in the overlap integral may be accurately inferred. The overlap integral appears to be constant within $\sim 6\%$ at beam energies above ~ 1.0 keV and within $\sim 10\%$ below 1.0 keV (Savin et al. 1999, in preparation). The overlap tests are done using argon instead of iron because it is difficult to get a large fraction of H-like and bare iron. However, the trapping conditions for iron were similar to those for argon. We thus expect the overlap integral for iron should also remain nearly constant. For DE and RE, possible residual changes in the overlap integral introduce negligible uncertainties in the measured cross sections and rate coefficients. For the DR satellites, there could be, at most, a $\sim 10\%$ underestimation of these quantities due to this effect.

As mentioned earlier, as no absolute cross section measurements are available with the present technique, the results are normalized to theoretical cross sections. We use the *R*-matrix calculation of the $3d_{5/2} \rightarrow 2p_{3/2}$ cross sections (Berrington & Tully 1997) at energies between 2.0 and 3.0 keV as the normalization. The fact that different theoretical calculations agree within 5% for this transition in this energy range (see § 4) and the high statistical quality of our measurements for this line ensure a reliable normalization. One disadvantage of this choice is that cascades from higher levels may contribute in that energy range. Their contributions from up to $n = 7$ levels are included using cross sections calculated by HULLAC. *R*-matrix calculations (Berrington & Tully 1997) are not available for $n > 4$ levels. A comparison of the cross sections for $n = 4$ levels shows that HULLAC, Zhang, Sampson, & Fortes 1990b and *R*-matrix all agree to within 10%. The polarizations of the cascade contributions are assumed to be zero because cascades tend to depolarize the radiation. Considering that the cascades contribute $\lesssim 15\%$ to the $3d_{5/2} \rightarrow 2p_{3/2}$ line emission in the normalization energy range, the errors in the cross sections for $n \geq 4$ introduce an insignificant uncertainty in the normalization level. Cascades also introduce an insignificant uncertainty to the polarization

TABLE 2

UNCERTAINTIES FOR MEASURED RATE COEFFICIENTS[a]

	$3p_{3/2} - 2s_{1/2}$ (%)[b]		$3p_{1/2} \rightarrow 2s_{1/2}$ (%)[b]		$3d_{5/2} \rightarrow 2p_{3/2}$ (%)[b]	
Source[c]	DR	DE+RE	DR	DE+RE	DR	DE+RE
Statistics	8	3	15	5	4	2
Polarization	8	2	0	0	8	2
Overlap	10	6	10	6	10	6
Line Blend	0	0	0	0	2	2
Quad. Sum.....	15	7	18	8	10	7

[a] Only the contributions within our measured energy range are included. The uncertainties in rate coefficients depend on temperature in principle, the numbers quoted here are for temperatures of $\sim$ 1.7 keV, near where the Fe^{23+} fractional abundance peaks in collisionally ionized plasmas.

[b] For each transition, the first column are the typical uncertainties of DR satellite contributions, and the second column are those of DE plus RE contributions. The uncertainties in the normalization, which only shift the entire data set without changing its shape, are the same as those for cross sections.

[c] The meaning of source terms is the same as in Table 1.

correction factor. The $3d_{5/2} \rightarrow 2p_{3/2}$ transition blends with the $3d_{3/2} \rightarrow 2p_{3/2}$ line. A 10% contribution from the $3d_{3/2} \rightarrow 2p_{3/2}$ transition is subtracted out and the uncertainties introduced should be $\lesssim 2\%$. The $3p_{3/2} \rightarrow 2s_{1/2}$ and $3p_{1/2} \rightarrow 2s_{1/2}$ transitions have higher photon energies than $3d_{5/2} \rightarrow 2p_{3/2}$, and the transmittances of the spectrometer and detector windows are higher. These effects are accounted for using the theoretical calculations, which introduces an uncertainty of $\sim 4\%$ in the normalization for these two transitions (Savin et al. 1996).

To calculate EIE rate coefficients appropriate to Maxwellian electron energy distributions, we weight each measured, normalized spectrum versus beam energy by the appropriate Maxwellian factor for the temperature being modeled, and sum the spectra to produce pseudo-Maxwellian line emission spectra. The contributions to the rate coefficients within our measured energy range are then extracted from the resulting line intensities. The contribution of the high-energy tail above the range of our measurements is estimated using the various theoretical calculations, all of which agree well with each other. The DR satellite spectra are averaged separately to yield estimates of their individual contributions. The rate coefficients can be deduced with much higher statistical precision than the individual cross sections, since all of the data are used in the calculation.

Tables 1 and 2 and summarize the various error sources discussed above.

4. RESULTS

In Figure 3 we show the observed line ratios, $(3p_{3/2} \rightarrow 2s_{1/2})/(3d_{5/2} \rightarrow 2p_{3/2})$, and $(3p_{1/2} \rightarrow 2s_{1/2})/(3d_{5/2} \rightarrow 2p_{3/2})$ summed over beam energies between 2.0 and 3.0 keV. Since the ratios from the two different spectrometers are consistent with each other, in the results presented below, we take the average of results from both spectrometers. All theoretical predictions agree well with each other and lie within the 1 σ error bars of the experimental data.

In Figure 4 we show the normalized cross sections for producing the $3p_{3/2} \rightarrow 2s_{1/2}$, $3p_{1/2} \rightarrow 2s_{1/2}$ and $3d_{5/2} \rightarrow 2p_{3/2}$ line emission. The error bars on the data points reflect 1 σ statistical uncertainties. The $3l5l'$ and $3l6l'$ DR resonances are well separated. All other DR resonances from ~ 1.0 keV to the EIE thresholds are unresolved and appear as a continuous increase in the cross sections. The RE feature at a beam energy of ~ 1.25 keV is produced by dielectronic capture into the $4l5l'$ level followed by autoionization to the $3p_{3/2}$, $3p_{1/2}$, or $3d_{5/2}$ levels of Fe XXIV. The feature at ~ 1.35 keV is associated with the dielectronic capture into $4l6l'$. The beam energy has a nearly Gaussian spread (Beiersdorfer et al. 1992). The FWHM is determined by fitting the $3l5l'$ DR peak of the $3d_{5/2} \rightarrow 2p_{3/2}$ transition and a value of 35 ± 5 eV is found. The various theoretical curves

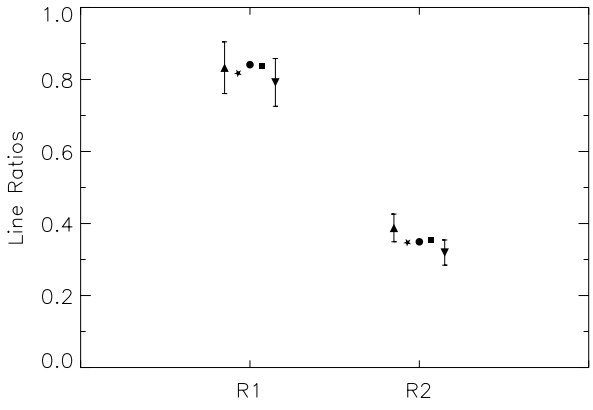

FIG. 3.—Line ratios in the normalization energy range, between 2.0 and 3.0 keV. R1 and R2 represent $(3p_{3/2} \rightarrow 2s_{1/2})/(3d_{5/2} \rightarrow 2p_{3/2})$ and $(3p_{1/2} \rightarrow 2s_{1/2})/(3d_{5/2} \rightarrow 2p_{3/2})$, respectively. *R*-matrix (Berrington & Tully 1997) calculations are shown by the circles, HULLAC calculations (Liedahl et al. 1995) by the stars, and those of Zhang et al. (1990b) by the squares. The triangles with error bars show the experimental results from the two spectrometers.

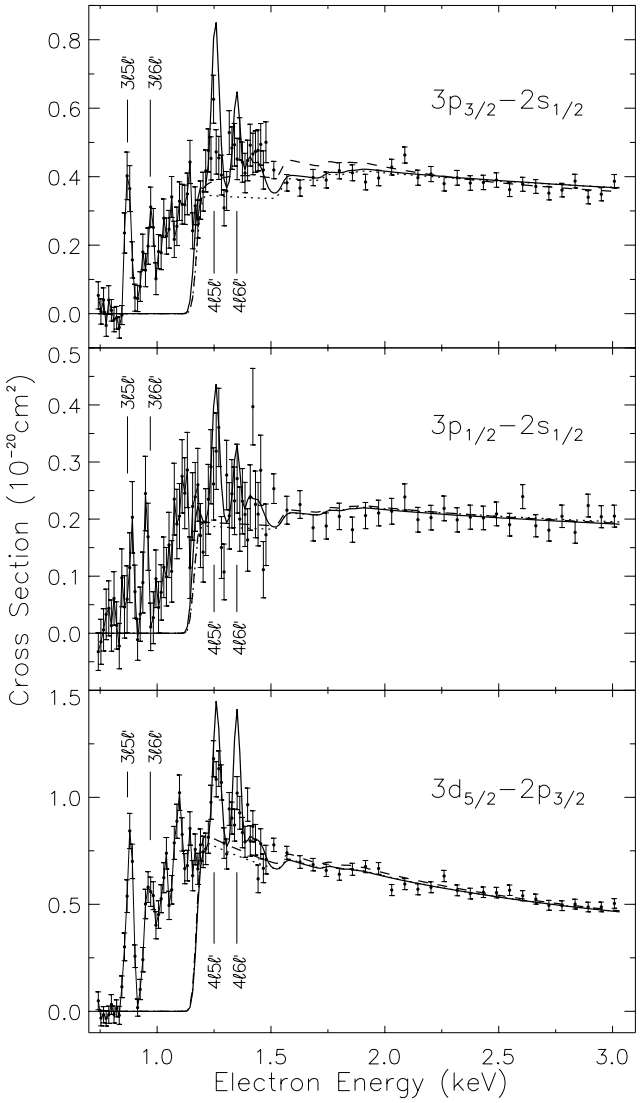

FIG. 4.—Cross sections for producing Fe XXIV line emission. The solid lines are the *R*-matrix calculations of DE and RE (Berrington & Tully 1997) plus HULLAC calculations for $n \leq 7$ cascade contributions. The dotted lines are the DW calculations of Zhang et al. (1990b) plus HULLAC calculations for cascades. The dashed lines are HULLAC calculations. The present *R*-matrix calculations are not shown here (see Fig. 7). Circles are the experimental results normalized to the theoretical values of the $3d_{5/2} \rightarrow 2p_{3/2}$ transition at the resonance-free energies, 2.0–.0 keV. Below the thresholds, line emission is due to DR satellites for electrons captured into $n \geq 5$ Rydberg levels. The data points at energies above ~ 1.5 keV have been rebinned to have ~ 55 eV bin size for clarity. Those below ~ 1.5 keV have ~ 11 eV bin size. The labels for resonances denote the configurations of the resonant states.

are convolved with the beam energy distribution for comparison with the data. The contributions of cascades to the effective cross sections are included for $n \leq 7$ in the theoretical curves using HULLAC calculations.

In Figure 5 we show the EIE rate coefficients that result from a Maxwellian average of our data in the energy range between the EIE thresholds and 3.0 keV and adding the contribution from the high-energy tail of the cross sections above 3.0 keV based on values calculated using HULLAC. The error bars show the 1 σ statistical uncertainties. The results are compared with the theoretical rate coefficients. Cascades from $n \leq 7$ are included when calculating the theoretical rates. To within the total experimental uncertainties, all theoretical calculations are consistent with our measurements. Both DW calculations are smaller than the *R*-matrix value owing to the lack of RE contributions in the DW calculations. The RE contributions, however, are only $\lesssim 5\%$ of the total rate coefficients, even smaller than the uncertainties of the measurements.

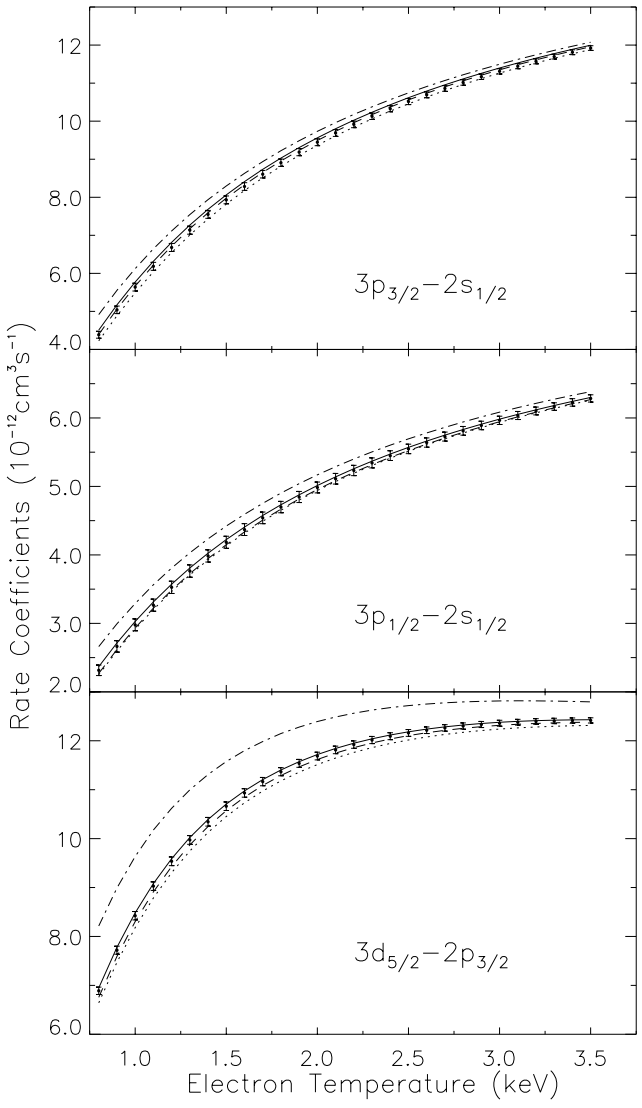

FIG. 5.—Rate coefficients for producing Fe XXIV line emission. The solid lines are the *R*-matrix calculations of DE and RE plus HULLAC calculations for $n \leq 7$ cascade contributions. The dotted lines are the calculations of Zhang et al. (1990b) plus HULLAC calculations for $n \leq 7$ cascades. The dashed lines are HULLAC calculations. Circles are our experimental results plus HULLAC calculations for the contributions of high-energy tail beyond our measurements. The dash-dotted lines are the total effective rate coefficients including the measured contributions of DR satellites with the captured electron in $n \geq 5$ levels.

The contributions of the DR satellites to the rate coefficients are calculated by including the experimental data at energies below the EIE thresholds in the Maxwellian average. The result is shown in Figure 5 as the dot-dashed curve. This contribution increases the rate coefficients by $\lesssim 10\%$, at temperatures near where Fe^{23+} fractional abundance peaks in collisionally ionized plasmas ($kT_e \sim 1.7$ keV, Arnaud & Raymond 1992), consistent with the findings of Liedahl et al. (1995).

5. DISCUSSION

To within the experimental uncertainties, excellent agreement is found between the cross sections from *R*-matrix, DW calculations, and our measurements. This shows that the DW is sufficient to reproduce the measurements even at energies near the thresholds of the transitions, except that DW calculations do not account for RE contributions. Fortunately, in collisionally ionized plasmas, RE contributes $\lesssim 5\%$ to the total line emission at temperatures where Fe^{23+} is abundant. The spectrally unresolved high-*n* DR satellites, however, make important contributions. The DR satellites in our measurements only include those with $n \geq 5$. They contribute $\lesssim 10\%$ of the total line emission at temperatures where Fe^{23+} is abundant in collisional equilibrium. The intensities of the high-*n* DR satellites have been estimated theoretically using

$$\alpha_{\rm DRS} = C_0\, A(x) B(z) f B \sqrt{E_{\rm th}}\, T^{-3/2} e^{-\beta(z) E_{\rm th}/T}\,, \qquad (5)$$

where f is the absorption oscillator strength, $E_{\rm th}$ is the EIE threshold of the main line in keV, B is the branching ratio for the satellites that is taken to be the branching ratio of the main line, T is the temperature in keV, and

$$A(x) = \frac{1}{1 + 0.105x + 0.015x^2}\,, \qquad (6)$$

$$B(z) = \frac{z^{1/2}(z+1)^2}{(z^2 + 13.4)^{1/2}}\,, \qquad (7)$$

$$\beta(z) = \frac{1}{1 + \delta[z^3/(1+z)^2]}\,, \qquad (8)$$

where $x = E_{\rm th}/E_{\rm H}(z+1)$ with $E_{\rm H} = 0.0136$ keV and z is the charge state of the recombining ion (Mewe & Gronenschild 1981). The parameter C_0 provides an average measure of the strength of the DR resonances, and δ adjusts the resonance energies. Mewe & Gronenschild (1981) give $C_0 = 3.9 \times 10^{-13}$ cm^3 s^{-1} and $\delta = 0.019$ for all DR satellites with $n \geq 3$. This estimate yields about twice our measured rates for $n \geq 5$ satellites. The $n = 3$ and 4 satellites, which are not sampled in our measurements, may contribute the rest of the line emission. Note that these satellite lines, however, will be resolved from the main Fe XXIV lines with the spectrometers on board *AXAF* and *XMM*.

Although the DW calculations show reasonable accuracy, they have not been completely incorporated into the commonly used spectral synthesis models. Liedahl et al. (1995) showed that Raymond & Smith (1977; hereafter RS) and Mewe, Gronenschild, & van den Oord (1985; hereafter

MEKA) underestimate the $3 \rightarrow 2$ line emission of Fe XXIV, XXIII by $\sim 30\%$. The HULLAC calculations of Liedahl et al. were partially included in a new model (Mewe, Kaastra, & Liedahl 1995; hereafter MEKAL). However, the line emissivities were not revised completely according to the new calculations. The ratios of rate coefficients from MEKAL and HULLAC are compared in Figure 6. Cascades are included by a temperature-independent constant, as is done in MEKAL. The values from MEKAL are $\sim 20\%$ lower than those from HULLAC at temperatures where the Fe^{23+} abundance peaks. The origin of this discrepancy is that in revising the iron L-shell atomic physics, the cross sections were simply scaled to the new calculations at an energy equal to the temperature at which the ion abundance peaks without also correcting the energy dependence. If the MEKAL rates for other Fe-L ions are similarly lower, iron abundance measurements previously determined using MEKAL from L-shell spectra may be incorrect. MEKAL also does not include RE, and it only incompletely accounts for DR satellite lines. Only DR satellites close to those transitions with ground states as lower levels are included for Fe XVII–XXII and Fe XXIV. Our measurements show that the DR satellites of the $3d_{5/2} \rightarrow 2p_{3/2}$ transition, whose lower level is not the ground level, are equally or more important than those of $3p_{3/2} \rightarrow 2s_{1/2}$ and $3p_{1/2} \rightarrow 2s_{1/2}$ transitions, as was first predicted theoretically by Zhdanov (1982).

Neglecting RE and approximating DR satellites using equation (5) may be sufficient for collisionally ionized plasmas, but in situations where the ionization balance is not solely determined by the electron temperature, e.g., in recombining or photoionized plasmas, RE and DR satellites may be more important and need to be accurately accounted for. In Figure 7, we show the cross sections at electron energies below 1.6 keV, where resonances are most important. None of the theoretical calculations used in the present analysis includes DR satellites, and we therefore examine only RE here. Neither of the DW calculations include resonant effects, and these are effective only in approximating the "base" level of the line emission. The *R*-matrix calculations of Berrington & Tully (1997) and the new *R*-matrix calculations presented here, however, take into account the RE associated with the autoionizing levels

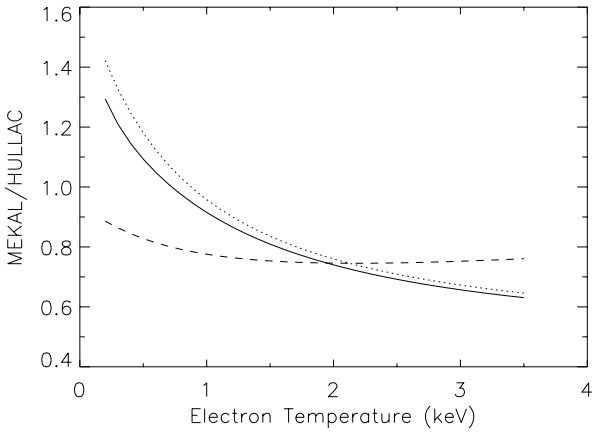

FIG. 6.—Comparison between the HULLAC rate coefficients and MEKAL model. The solid line is for the $3p_{3/2} \rightarrow 2s_{1/2}$ transition, the dotted line is for the $3p_{1/2} \rightarrow 2s_{1/2}$ transition, and the dashed line is for the $3d_{5/2} \rightarrow 2p_{3/2}$ transition.

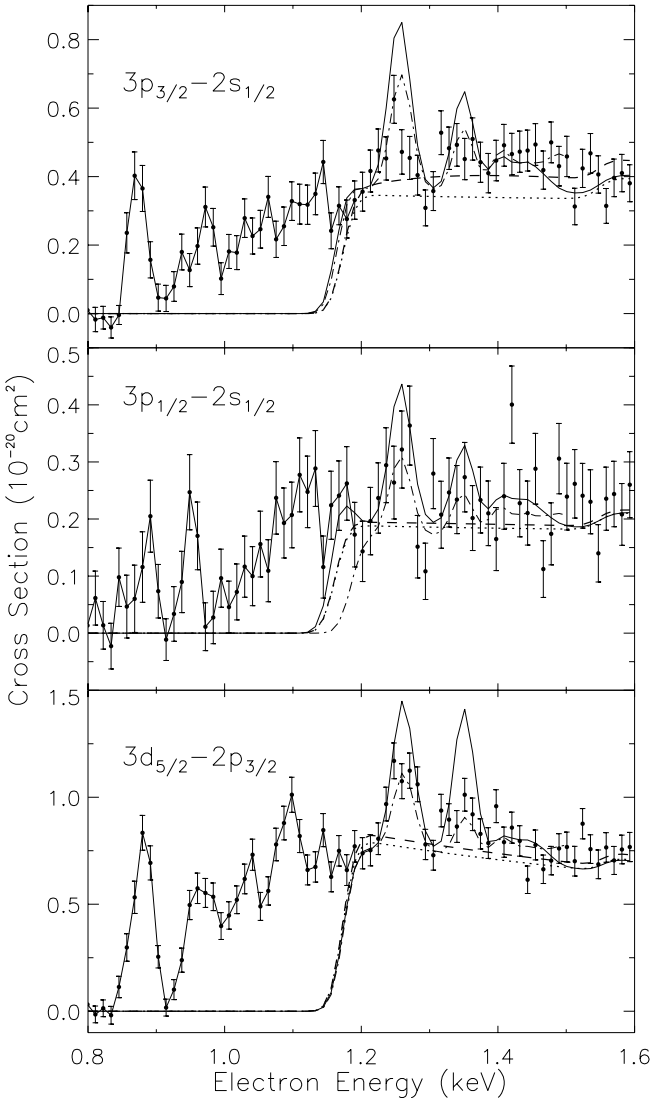

FIG. 7.—Cross sections at electron energies below 1.6 keV showing the resonance structure in the line excitation. The solid lines are the *R*-matrix calculations of Berrington & Tully. The dash-dotted lines are the present *R*-matrix calculations. The dotted lines are the calculations of Zhang et al. (1990b). The dashed lines are HULLAC calculations. The circles are our normalized experimental results. The increase of the cross sections above 1.5 keV is due to the onset of cascades. The present *R*-matrix calculations only extend to the electron energy at ~ 1.5 keV. No calculations are available for the DR resonance contributions below threshold.

of type $3lnl'$ and $4lnl'$. The $3lnl'$ resonances occur at energies very close to the EIE thresholds and are hardly noticeable after being convolved with the beam energy spread. It is interesting to note that considerable discrepancies exist between Berrington & Tully and the present calculations for the $4lnl'$ resonances. The cross sections of Berrington & Tully tend to be larger than the present calculations and the experimental data for the $4l5l'$ and $4l6l'$ resonances. To understand the origin of this discrepancy, we show the detail of $4l5l'$ resonances for both calculations in Figure 8. In addition to some apparent shift of the resonance energies, it is clear that the energy grid used in Berrington & Tully is too coarse, which results in the less complicated structure and overestimation of the resonance effects after being convolved with the beam energy spread. At electron

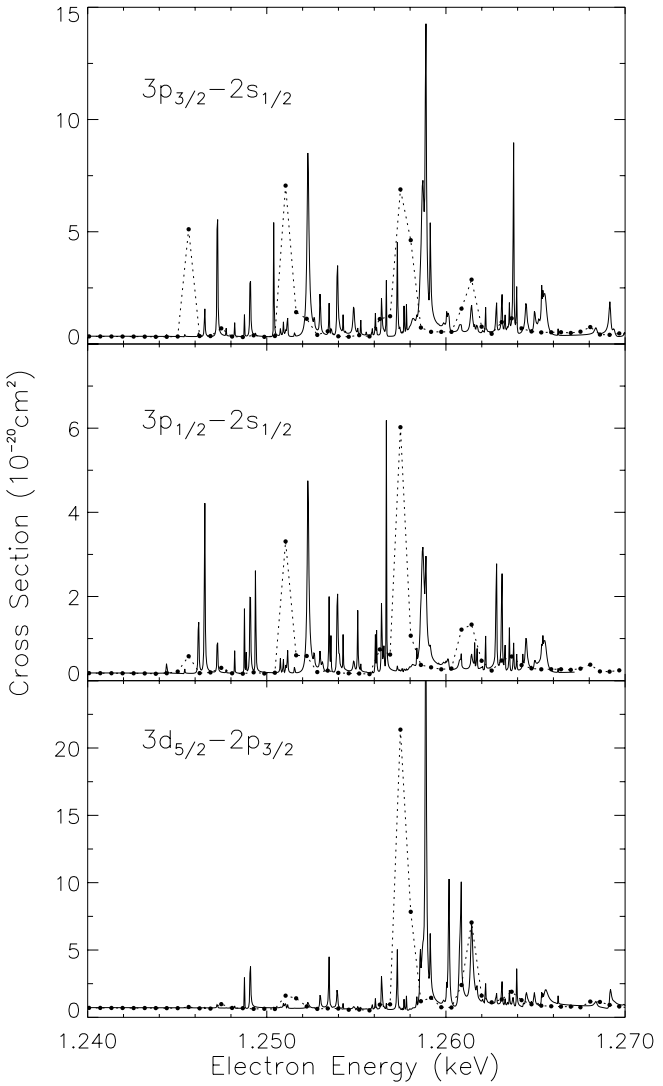

FIG. 8.—The detailed structure of the $4l5l'$ resonances. The solid lines are our present R-matrix calculations. The dotted lines are the R-matrix calculations of Berrington & Tully (1997), and the circles indicate their energy grid.

energies close to 1.5 keV, the cross sections of Berrington & Tully are smaller than the present calculations and the experimental data.

6. CONCLUSIONS

We have measured the relative cross sections for producing Fe XXIV $3d_{5/2} \rightarrow 2p_{3/2}$, $3p_{3/2} \rightarrow 2s_{1/2}$, and $3p_{1/2} \rightarrow 2s_{1/2}$ transitions at the electron energies between 0.7 and 3.0 keV. Good agreement with R-matrix and DW calculations is found. However, the atomic data incorporated in standard spectral synthesis models (RS, MEKA, and MEKAL) only partially include these recent calculations.

In collisionally ionized plasmas, at temperatures where Fe^{23+} is abundant, RE contributions are $\lesssim 5\%$ of the total line emission, while spectrally unresolved DR satellites with $n \geq 5$ contribute $\lesssim 10\%$. The contributions from $n = 3$ and 4 DR satellites are also expected to be nonnegligible. But unlike the $n \geq 5$ satellites, these are expected to be resolved with *AXAF* and *XMM*. In situations where the ionization balance is not solely determined by the kinetic temperature of the plasma, such as in recombining or photoionized plasmas, RE and DR satellites may contribute a considerable fraction of the line emission.

The authors wish to thank S. T. Manson, J. S. Kaastra, and R. Mewe for useful discussions and P. A. D'Antonio, E. W. Magee, and D. H. Nelson for their expert technical support. The authors also would like to thank K. A. Berrington and H. L. Zhang for providing their data in electronic form. Work at Lawrence Livermore National Laboratory was performed under the auspices of the US Department of Energy under contract W-7405-ENG-48. This program is supported by a NASA High Energy Astrophysics X-Ray Astronomy Research and Analysis grant NAGW-4185 (Columbia University) and work order W-19127 (LLNL). The work at Kansas State University is supported by Division of Chemical Science, Office of Basic Energy Research, US Department of Energy.

REFERENCES

Arimoto, N., Matshushita, K., Ishimaru, Y., Ohashi, T., & Renzini, A. 1997, ApJ, 477, 128
Arnaud, M., & Raymond, J. 1992, ApJ, 398, 394
Beiersdorfer, P., et al. 1990, Phys. Rev. Lett. 65, 1995
———. 1992, Phys. Rev. A, 46, 3812
Beiersdorfer, P., Crespo López-Urrutia, J. R., Föster, E., Mahiri, J., & Widmann, K. 1997, Rev. Sci. Instrum. 68, 1077
Beiersdorfer, P., & Wargelin, B. J. 1994, Rev. Sci. Instrum. 65, 13
Berrington, K. A., & Tully, J. A. 1997, A&AS, 126, 105
Brown, G. V., Beiersdorfer, P., & Widmann, K. 1998, Rev. Sci. Instrum., 70, 280
Brown, I. G., Galvin, J. E., MacGill, R. A., & Wright, R. T. 1986, Appl. Phys. 49, 1019
Fabian, A. C., et al. 1994, ApJ, 436, L63
Gu, M. F., Savin, D. W., & Beiersdorfer, P. 1998, Phys. Rev. A, in preparation
Henke, B. L., Gullikson, E. M., & Davis, J. C. 1993, Atom. Data Nucl. Data Tables, 54, 181
Inal, M. K., & Dubau, J. 1989, J. Phys. B, 22, 3329
Kahn, S. M., & Liedahl, D. A. 1990, in Iron Line Diagnostics in X-ray Sources, ed. A. Treves, G. C. Perola, & L. Stella (Berlin: Springer), 3
Knapp, D. A., et al. 1993, Phys. Rev. A, 47, 2039
Levine, M. A., et al. 1988, Phys. Scr., T22, 157
Liedahl, D. A., Osterheld, A. L., & Goldstein, W. H. 1995, ApJ, 438, L115
Makino, F., & Mitsuda, K. 1997, X-ray Imaging and Spectroscopy of Cosmic Hot Plasmas (Tokyo: Universal Academy)
Mewe, R., & Gronenschild, E. H. B. M. 1981, A&AS. 45, 11
Mewe, R., Gronenschild, E. H. B. M., & van den Oord, G. H. J. 1985, A&AS, 62, 197
Mewe, R., Kaastra, J. S., & Liedahl, D. A. 1995, Legacy, 6, 16
Percival, I. C., & Seaton, M. J. 1958, Philos. Trans. R. Soc. London, A, 251, 113
Raymond, J. C., & Smith, B. W. 1977, APJS, 35, 419
Saloman, E. B., Hubbel, J. H., & Scofield, J. H. 1988, Atom. Data Nucl. Data Tables, 38, 1
Savin, D. W., et al. 1996, ApJ, 470, L73
———. 1999, in preparation
Scofield, J. H. 1989, Phys. Rev. A, 40, 3054
———. 1991, Phys. Rev. A, 44, 139
Zhang, H. L., Sampson, D. H., & Clark, R. E. H. 1990a, Phys. Rev. A, 41, 198
Zhang, H. L., Sampson, D. H., & Fontes, C. J. 1990b, Atom. Data Nucl. Data Tables, 44, 31
Zhdanov, V. P. 1982, J. Phys. B, 15, L541